Materials Today Physics 63 (2026) 102072

Contents lists available at ScienceDirect

Materials Today Physics

journal homepage: www.journals.elsevier.com/materials-today-physics

Large piezo-valley in a Janus Mo_2S_2O altermagnet with high thermoelectric performance

Fazle Subhan [a], Luqman Ali [b], Zhansheng Lu [c,*], Joonkyung Jang [a,**]

[a] Department of Nanoenergy Engineering, Pusan National University, Busan, 46241, Republic of Korea
[b] Department of Pharmacology, University of Virginia, Charlottesville, VA, 22903, USA
[c] College of Mathematics and Physics, Beijing University of Chemical Technology, Beijing, 100029, China

ARTICLE INFO

Keywords:
Altermagnetism
Piezo-valley effect
Piezoelectricity
Thermoelectric properties

ABSTRACT

Altermagnets represent an emerging class of magnetic materials that exhibit symmetry-protected spin splitting while maintaining zero net magnetization, offering new opportunities for spin- and valley-based functionalities. In this work, a two-dimensional Janus Mo_2S_2O monolayer is identified as a polar semiconducting altermagnet that combines robust magnetic, electromechanical, and thermoelectric properties. The system stabilizes in a compensated antiferromagnetic ground state with a Néel temperature around 550 K, ensuring magnetic stability well above room temperature. Its electronic structure reveals a band gap of 1.15 eV together with strong momentum-dependent spin splitting of nearly 300 meV at the X and Y valleys. Uniaxial strain effectively breaks the in-plane symmetry and induces a giant piezo-valley polarization, producing valence-band valley splittings reaching 334 meV. The polar Janus geometry further gives rise to a strong out-of-plane piezoelectric response, with a piezoelectric coefficient d_{31} of 16.2 p.m./V, highlighting significant electromechanical coupling. Thermoelectric transport calculations demonstrate a large Seebeck coefficient of 1.52 mV K^{-1} at 300 K, suppressed lattice thermal conductivity, and a thermoelectric figure of merit approaching 0.97 at 500 K. These combined properties establish Janus Mo_2S_2O as a promising platform for strain-controlled spin-valley devices and low-temperature waste-heat energy conversion.

1. Introduction

A large fraction of the thermal energy produced in industrial and domestic processes is released at relatively low temperatures, typically in the range of 300 K – 520 K. This low-grade heat can constitute more than half of the total waste heat generated, yet it is notoriously difficult to utilize efficiently due to the limited temperature gradient available [1,2]. Thermoelectric materials provide a solid-state approach to directly convert such temperature differences into electrical power, offering advantages such as the absence of moving parts, silent operation, and long-term operational stability [3–5]. The performance of a thermoelectric material is quantified by the dimensionless figure of merit, ZT. Achieving a high ZT requires a delicate balance: a large power factor ($S^2\sigma$) combined with a low thermal conductivity. Because the electronic transport coefficients S, σ, and the electronic contribution to thermal conductivity κ_e are all closely linked to the electronic band structure, improving one parameter often adversely affects the others. In contrast, the lattice thermal conductivity (κ_l) is more amenable to independent tuning. Various strategies such as chemical alloying [6], interface and nanostructure engineering [7], and enhanced lattice anharmonicity [8] have been successfully employed to suppress κ_l by increasing phonon scattering.

Conventional thermoelectric materials such as Bi_2Te_3 and PbTe typically exhibit ZT values close to unity under practical conditions [9]. However, large-scale waste heat recovery applications demand significantly higher efficiencies, generally corresponding to ZT ≈ 2 or above [10]. Many magnetic materials struggle to reach this regime because strong magnetic interactions often deteriorate charge transport [11–14]. Nevertheless, recent studies indicate that magnetic order can partially relax the intrinsic coupling between S, σ, and κ_e, opening new pathways for enhancing thermoelectric performance [15–23]. For instance, substituting only 1% Cr at the Bi sites in Bi_2Te_3 has been shown to substantially enhance the Seebeck coefficient and increase the ZT value by nearly 25% around 400 K [24]. Moreover, magnetic ordering can

* Corresponding author.
** Corresponding author.
E-mail addresses: zslu@buct.edu.cn (Z. Lu), jkjang@pusan.ac.kr (J. Jang).

https://doi.org/10.1016/j.mtphys.2026.102072
Received 15 January 2026; Received in revised form 18 February 2026; Accepted 10 March 2026
Available online 12 March 2026

intensify spin–phonon coupling, which strengthens phonon scattering and reduces κ_l, further benefiting the overall thermoelectric efficiency [25–27]. Recently, a new class of magnetic materials known as altermagnets has attracted considerable interest. These systems display symmetry-protected spin splitting in their electronic bands while maintaining a fully compensated magnetic order and zero net magnetization [28]. Such an unconventional electronic structure suggests the potential for unusual charge and heat transport phenomena. A notable example is RuO_2, an experimentally confirmed altermagnet that has been reported to exhibit anomalous thermal transport behavior [29]. Despite these intriguing features, the thermoelectric properties of altermagnets remain largely unexplored. At the two-dimensional limit, several materials have been theoretically predicted to host altermagnetic order arising from a special form of antiferromagnetic arrangement. Representative examples include Cr_2O_2 and V_2Se_2O [30–32], where pronounced spin splitting emerges even though the total magnetic moment vanishes. However, these systems preserve inversion symmetry, which prohibits a finite piezoelectric response. As a result, they cannot exhibit coupled piezoelectric and altermagnetic functionalities. This limitation motivates the search for two-dimensional materials that simultaneously host altermagnetism and piezoelectricity, a combination referred to as two-dimensional piezoelectric altermagnetism. Identifying such materials is both scientifically significant and technologically challenging.

Encouraging insights can be drawn from related material classes. Several two-dimensional piezoelectric have already been proposed, where magnetic order and piezoelectricity coexist [33,34]. A common feature of many of these systems is a Janus structure, in which different atomic species occupy the top and bottom surfaces of the monolayer. This structural asymmetry breaks out-of-plane mirror symmetry and naturally induces a strong piezoelectric response [35]. Another critical aspect concerns the control of spin polarization in two-dimensional altermagnets. Although these materials possess compensated magnetic order, external stimuli are often required to activate spin-polarized electronic states. Among various approaches, mechanical strain is particularly effective. By modifying lattice parameters and magnetic exchange interactions, strain can induce sizable spin polarization and enhance the intrinsic altermagnetic spin splitting. Consequently, strain engineering represents a powerful and practical strategy for tuning the functional properties of two-dimensional piezoelectric altermagnets. In this work, we investigate the two-dimensional altermagnetic Janus material Mo_2S_2O. Our results reveal that this system exhibits an exceptionally high thermoelectric figure of merit, reaching $ZT \approx 0.97$ at 500 K. In addition, the predicted Néel temperature of approximately 550 K confirms that the antiferromagnetic order remains stable throughout the entire operating temperature range. Beyond its thermoelectric performance, Mo_2S_2O also displays a pronounced piezo-valley effect, where mechanical strain induces a substantial energy splitting between inequivalent valleys. This strong coupling between lattice deformation and valley polarization offers an additional degree of control over charge and spin transport. The coexistence of robust altermagnetism, large piezo-valley polarization, and high thermoelectric efficiency highlights Janus Mo_2S_2O as a highly promising multifunctional material for low-temperature waste heat recovery and valley-controlled nanoelectronic applications.

2. Computational section

All first-principles calculations were carried out using the Vienna Ab initio Simulation Package (VASP) [36]. To properly describe the localized character of the Mo-3d states, electron–electron correlations were treated using the GGA + U approach, with an effective on-site Coulomb interaction of U = 3.5 eV, in agreement with earlier theoretical investigations on Mo-based compounds [37]. A plane-wave energy cutoff of 850 eV was adopted to ensure high numerical accuracy in total energies and interatomic forces. The Brillouin zone of the two-dimensional system was sampled using a 15 × 15 × 1 Monkhorst–Pack k-point grid, providing sufficient resolution for electronic structure calculations. Structural relaxations were performed until the Hellmann–Feynman forces on all atoms were reduced below 0.01 eV $Å^{-1}$, while electronic self-consistency was achieved with an energy tolerance of 10^{-6} eV. To eliminate artificial interactions between periodically repeated layers, a vacuum spacing of 25 Å was introduced along the out-of-plane direction. Dynamical stability was assessed through phonon dispersion calculations within the framework of density functional perturbation theory. The force constants obtained from the optimized geometry were analyzed using the Phonopy package [38]. The magnetic ground state was determined by comparing the total energies of various collinear magnetic configurations, including both ferromagnetic and antiferromagnetic arrangements. All electronic band structures were subsequently calculated using the fully relaxed equilibrium lattice. Thermoelectric transport properties were evaluated using semiclassical Boltzmann transport theory under the constant relaxation-time approximation, as implemented in the BoltzTraP code [39]. This approach enables a reliable description of temperature-dependent carrier transport in low-dimensional materials and has been extensively employed in previous theoretical studies of quantum thermoelectric. The lattice thermal conductivity was evaluated using the Phono3py package by computing third order interatomic force constants. A 3 × 3 × 1 supercell was employed to properly account for anharmonic phonon interactions. All calculations used a strict total energy convergence threshold of 10^{-8} eV, and atomic positions were fully relaxed until the residual forces on each atom were below 0.001 eV $Å^{-1}$. Beside the K-grid of 150 × 150 × 1 is used. These settings ensure an accurate description of phonon scattering and reliable lattice thermal conductivity results.

3. Results and discussion

Fig. 1(a)–(b) show the top and side views of the optimized Mo_2S_2O Janus monolayer, respectively. The structure crystallizes in a tetragonal lattice with space group *P4mm* (No. 99) and an optimized in-plane lattice constant of 4.17 Å. The Janus character arises from the broken out-of-plane mirror symmetry due to the asymmetric distribution of anions, with sulfur and oxygen atoms located on opposite sides of the monolayer. Each Mo atom is coordinated by both O and S atoms, forming a distorted octahedral environment in which O atoms occupy the axial positions while S atoms lie predominantly in the equatorial plane. The Mo–O bonds are shorter than the Mo–S bonds, reflecting the stronger covalent interaction between Mo and O. This polar Janus configuration ensures structural stability and is expected to significantly influence the electronic, magnetic, and spin-dependent properties of the monolayer. To identify the magnetic ground state of the Janus Mo_2S_2O monolayer, we compared the total energies of the ferromagnetic (FM) and antiferromagnetic (AFM) spin configurations. In AFM case we consider one Mo is up while one is down. The AFM state is found to be 566 meV lower in energy than the FM state, confirming a robust antiferromagnetic ground state and indicating strong magnetic exchange interactions. Such a large energy difference suggests that the AFM ordering is stable against thermal fluctuations. In this Janus system, the total magnetic moment of the unit cell is zero, reflecting the compensated antiferromagnetic ordering, while the local magnetic moment on the Mo atom is calculated to be 2.4 μ_B. The phonon dispersion curve, shown in Fig. 1 (c), exhibits no imaginary frequencies throughout the Brillouin zone, demonstrating the dynamical stability of the optimized Janus monolayer [40]. In addition, the formation energy is calculated to be −2.041 eV/atom, indicating strong thermodynamic stability and confirming that the structure is energetically favorable relative to its constituent elements. These results collectively verify that the Mo_2S_2O Janus monolayer is magnetically, dynamically, and thermodynamically stable, providing a reliable foundation for further exploration of its electronic, magnetic, and spin-dependent properties. To further examine the stability of the

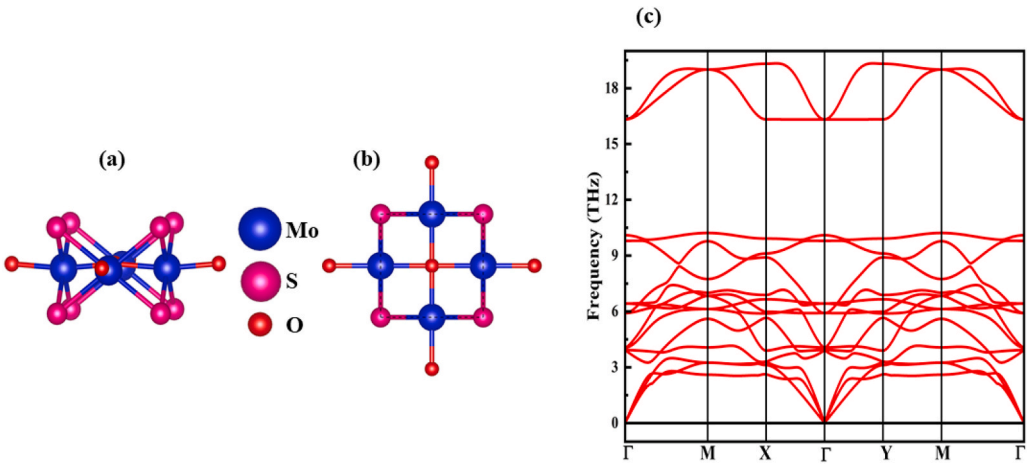

Fig. 1. Side (a) and top (b) views of the optimized Janus Mo_2S_2O monolayer crystal structure, together with the calculated phonon dispersion along high-symmetry directions (c). The absence of imaginary phonon modes confirms the dynamical stability of the Janus Mo_2S_2O monolayer.

antiferromagnetic ordering, the Néel temperature of the system was estimated by evaluating the temperature-dependent sublattice magnetization, n(T), using the VAMPIRE atomistic spin dynamics simulation framework. The magnetic interactions were modeled using a classical Heisenberg Hamiltonian, explicitly incorporating the effect of single-ion magnetic anisotropy, which can be written as

$$H_{ex} = -\sum_{i \neq j} J_{ij}\left(S_i \cdot S_j\right) - k_u (S_i \cdot e)^2 \quad (1)$$

$$n_\alpha = \frac{1}{N_\alpha}\sum_{i}^{N_\alpha} S_i \quad (2)$$

In these equations, J_i represents the magnetic exchange coupling between neighboring spins located at sites i and j, while S_i denotes the orientation of the magnetic moment at site i. The constant k_u is the single-ion anisotropy parameter, e defines the easy-axis direction, n_α corresponds to the mean magnetization of the α sublattice, and N_α is the total number of magnetic atoms belonging to that sublattice. The exchange coupling strength J_{ij} was determined from first-principles calculations using the expression $J_{ij} = E/(Nm^2)$, where E_{ex} is the total energy difference between the ferromagnetic and antiferromagnetic states, N denotes the number of magnetic atoms in the unit cell, and m is the average local magnetic moment per atom. The thermal evolution of the magnetic order was investigated through field-cooled simulations, in which the Landau–Lifshitz–Gilbert (LLG) equation of motion was numerically solved using the Heun integration algorithm as implemented in the VAMPIRE package. To minimize finite-size artifacts, a large 50 × 50 × 1 supercell was constructed, with periodic boundary conditions applied along the in-plane directions. Each temperature point was simulated for 1000000 steps, ensuring sufficient thermal equilibration and statistical accuracy. The resulting temperature dependence of the average sublattice magnetization $n(T)$ for the Mo_2S_2O monolayer is presented in Fig. 2. The discrete data points correspond to the simulation results, while the continuous curve represents a fit to the Curie–Bloch relation, $n(T) = [1 - T/T_N]^\beta$, using a critical exponent $\beta = 0.34$. From this fitting procedure, the Néel temperature of the system is estimated to be 550 K, indicating robust antiferromagnetic ordering persisting up to room temperature.

Fig. 3 shows the spin-resolved electronic band structure of the Janus Mo_2S_2O monolayer along the high-symmetry path. The system is a semiconductor with a band gap of 1.15 eV and exhibits a pronounced spin splitting of approximately 300 meV at the X and Y points, while maintaining a zero net magnetic moment. These features are characteristic of altermagnetism [41,42]. Although the magnetic ground state is collinear antiferromagnetic with fully compensated magnetization,

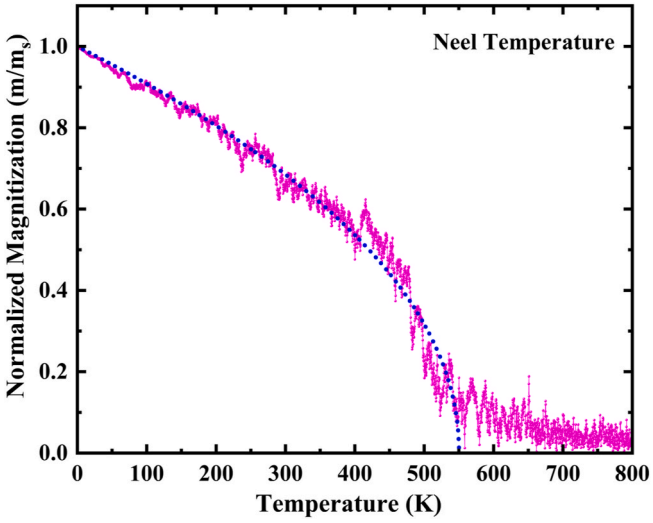

Fig. 2. Temperature dependence of the normalized sublattice magnetization of the Janus Mo_2S_2O monolayer obtained from atomistic spin dynamics simulations.

the spin-up and spin-down bands are clearly nondegenerate over most of the Brillouin zone, even in the absence of spin–orbit coupling (SOC). This momentum-dependent spin splitting arises from the combined effect of antiferromagnetic ordering and the reduced symmetry of the Janus structure, rather than from relativistic effects. As a result, opposite spin states are separated in energy at specific k-points, giving rise to large valley-dependent spin polarization. The coexistence of a sizable band gap, compensated antiferromagnetism, and strong spin splitting at high-symmetry points firmly establishes Janus Mo_2S_2O as a semiconducting altermagnet, making it a promising platform for spin- and valley-dependent electronic applications.

Building upon the altermagnetic electronic structure discussed above, we next analyze the valley characteristics of the Janus Mo_2S_2O monolayer. Examination of the electronic band dispersion reveals that the valence-band maxima at the X and Y valleys are energetically degenerate, indicating the absence of intrinsic spin-valley polarization in the unstrained system. This valley degeneracy is protected by the in-plane mirror symmetry (M_{XY}), which enforces equivalent electronic environments along the two orthogonal in-plane directions and therefore constrains the valley energies to be identical. Specifically, the mirror operation M_{xy}: (x, y, z) → (x, y, -z) leaves the crystal potential

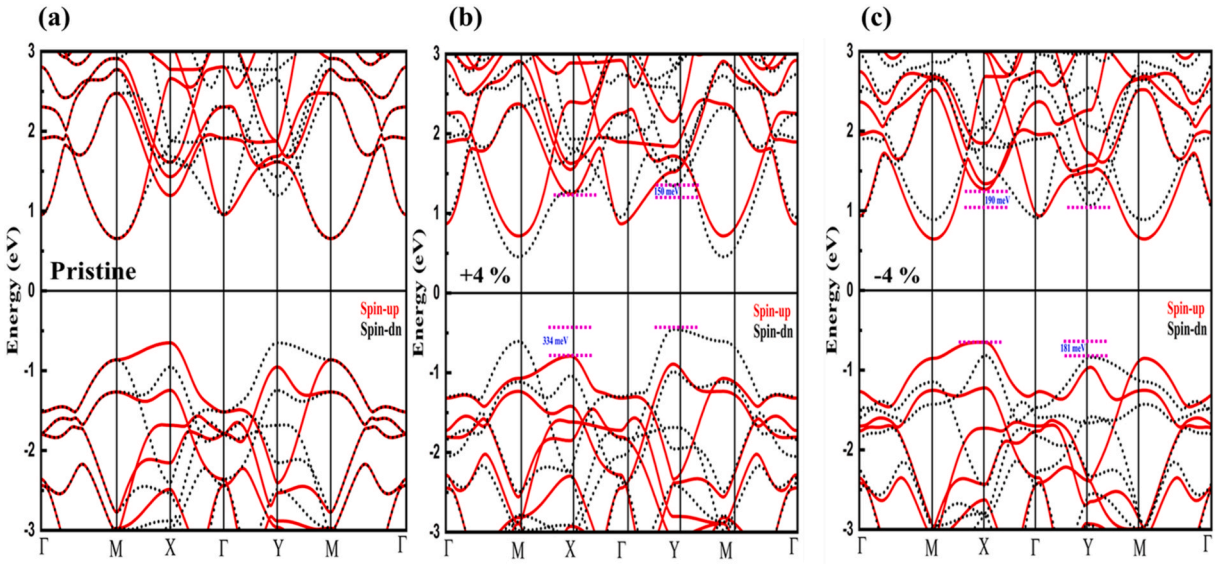

Fig. 3. Spin-resolved electronic band structures of the Janus Mo_2S_2O monolayer in the pristine state and under ±4% uniaxial strain, with red and black curves representing spin-up and spin-down channels, respectively.

invariant when the mirror plane is chosen at the center of the slab. In the presence of spin orbit coupling, the spin operator transforms as M_{xy} S M_{xy}^{-1} = (S_x, S_y, -S_z), which imposes symmetry restrictions on the spin resolved Hamiltonian. Because the Hamiltonian commutes with M_{xy}, the Bloch states at the X and Y valleys transform into symmetry equivalent partners, leading to E_v (X) = E_v (Y). As a consequence, although momentum dependent spin splitting is present due to altermagnetism, the valley resolved energies remain locked, and no net spin valley polarization emerges in the unstrained monolayer. To induce a finite spin-valley polarization, this symmetry constraint must be lifted. One effective and experimentally feasible route is the application of uniaxial strain, which breaks the in-plane symmetry by deforming the lattice anisotropically. Motivated by earlier reports on similar altermagnetic systems such as Cr_2O_2, we applied both compressive and tensile uniaxial strains along the X and Y directions of the Mo_2S_2O monolayer. The resulting strain-modified electronic band structures for 4% tensile and compressive strain are presented in Fig. 3(b)and(c), while the extracted strain-dependent valley energies are plotted in Fig. 4(a)and(b). Our calculations show that the magnitude of the valley splitting is identical for strain applied along either in-plane direction; however, the sign of the energy shift reverses between the X and Y valleys. This behavior originates from the directional nature of uniaxial strain: deformation along one crystallographic axis directly alters the orbital overlap and crystal-field environment at the corresponding valley, while inducing an opposite distortion along the perpendicular direction. Consequently, stretching or compressing the lattice along the x-direction raises (or lowers) the energy of the X valley while simultaneously lowering (or raising) the Y valley by an equal amount. A pronounced strain-induced valley splitting is observed in the Janus system. Under a moderate 4% compressive strain, the valence-band valley splitting reaches −334 meV, while the application of 4% tensile strain reduces the splitting to 181 meV. In the conduction band, the corresponding valley splittings are found to be 150 meV and −190 meV under 4% compressive and tensile strains, respectively.

Notably, these values are significantly larger than those reported for related Janus and layered materials, including V_2SeTeO (~200 meV) [43], V_2SeO [44], and V_2AsBrO (155 meV) [45], highlighting the exceptionally strong strain-valley coupling in the present system. From a

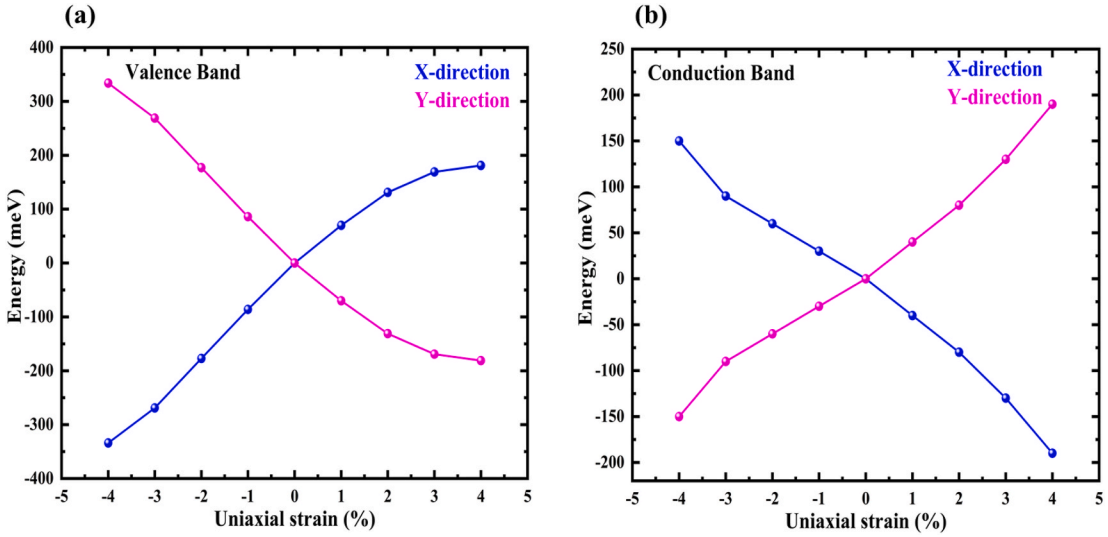

Fig. 4. Strain-dependent valley energy shifts of the Janus Mo_2S_2O monolayer in the (a) valence band and (b) conduction band along the X and Y directions.

microscopic perspective, this effect arises from the sensitivity of the electronic orbitals to lattice distortions, which modify the local bonding environment and crystal-field symmetry at the valley extrema. In the context of altermagnetism, where electronic bands are inherently spin-dependent, this strain-induced valley asymmetry naturally translates into a finite spin-valley polarization. As a result, strained Janus Mo_2S_2O emerges as a highly promising platform for valleytronic and piezo-spintronic applications, where mechanical deformation can be used to control spin-polarized valley states.

Subsequently, the electromechanical response of the Janus Mo_2S_2O monolayer was investigated to evaluate its piezoelectric behavior. Piezoelectricity manifests through two interrelated mechanisms: the direct effect, in which mechanical deformation generates an electrical polarization, and the converse effect, where an applied electric field produces a mechanical strain. Although these two processes describe different physical responses, they originate from the same constitutive relations and are therefore represented by equivalent piezoelectric tensors. In the present study, emphasis is placed on understanding how the intrinsic polarization of the material evolves under externally applied strain. This behavior is described by the piezoelectric strain coefficient d_{ij}, which connects the variation of polarization to mechanical deformation through the relation:

$$e_{ijk} = \frac{\partial P_i}{\partial e_{jk}} \tag{3}$$

Within first-principles calculations, however, the quantity that can be obtained directly is the piezoelectric stress tensor e_{ij}. While both d_{ij} and e_{ij} are third-rank tensors, the former links polarization to strain, whereas the latter relates polarization to applied stress. The transformation between these two representations requires knowledge of the crystal's elastic response, which is captured by the elastic compliance tensor S_{ij}. Once the elastic coefficients are available, the piezoelectric strain tensor can be derived from the stress tensor through the elastic stiffness matrix according to:

$$e_{ijk} = \sum_K C_{ijkl} . d_{kl} \tag{4}$$

Using the calculated piezoelectric stress coefficients in conjunction with the elastic constants, the strain-induced polarization response of Mo_2S_2O was determined. Based on symmetry considerations, the nonzero out-of-plane piezoelectric component e_{31} was evaluated. The calculated value of e_{31} is 0.24 pC/m, corresponding to a piezoelectric strain coefficient d_{31} of 1.62 p.m./V. This response is larger to that reported for Cr_2SeO (−1.17 p.m./V) and Cr_2SO (−0.97 p.m./V) [46], highlighting the enhanced piezoelectric performance of the Janus Mo_2S_2O monolayer.

Before discussing the thermoelectric properties, we first examine the role of electron and hole transport from a band-structure perspective. The electronic dispersion around the X and Y symmetry points exhibits nearly identical shapes, indicating similar transport characteristics along these two directions. Consistent with this observation, the calculated effective masses of both charge carriers are the same along the X and Y directions. The effective mass of electrons is found to be 0.15 m_0, while that of holes is 0.21 m_0 at both symmetry points. Owing to the comparable band curvature and effective masses at X and Y, the resulting thermoelectric response is expected to be directionally equivalent. Therefore, without loss of generality, we focus on the X direction to analyze the thermoelectric properties of the system. Fig. 5 illustrates the variation of the Seebeck coefficient of the MoS_2O altermagnet as a function of carrier concentration at temperatures of 300 K, 400 K, and 500 K. A clear sign change of the Seebeck coefficient is observed at the charge-neutrality point, separating hole-dominated transport in the negative carrier concentration region from electron-dominated transport in the positive region. This behavior confirms the intrinsic semiconducting nature of MoS_2O and its ability to support both p-type and n-type thermoelectric conduction. In the vicinity of the charge-neutrality point, the Seebeck coefficient reaches its maximum magnitude, attaining a peak value of approximately 1.52 mV K^{-1} at 300 K. As the carrier concentration increases on either side of neutrality, the magnitude of the Seebeck coefficient gradually decreases for both electrons and holes due to the enhanced carrier degeneracy and the reduced energy asymmetry around the Fermi level. Notably, for a fixed carrier concentration, the absolute value of the Seebeck coefficient systematically decreases with increasing temperature from 300 K to 500 K. This reduction originates from thermal broadening of the carrier distribution, which weakens the energy dependence of the transport coefficients and suppresses the entropy carried per charge carrier.

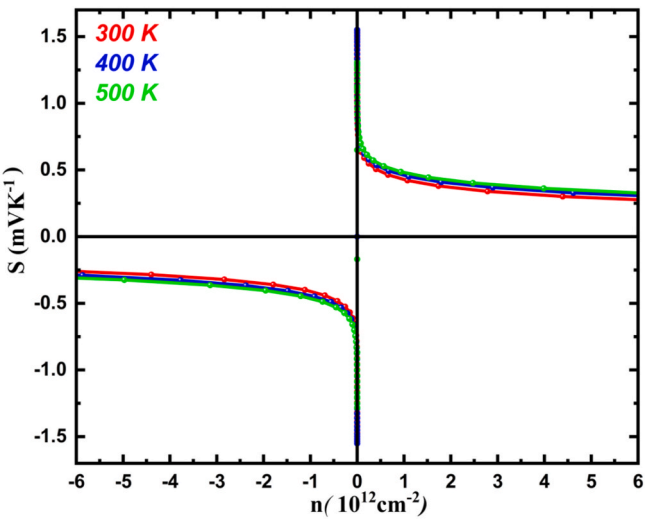

Fig. 5. Carrier-concentration dependence of the Seebeck coefficient of the Janus Mo_2S_2O monolayer at 300 K, 400 K, and 500 K.

Despite this decrease, the overall carrier-dependent trends remain unchanged across all temperatures, indicating stable thermoelectric behavior. The combination of a large Seebeck coefficient at room temperature and tunable bipolar transport highlights MoS_2O as a promising altermagnetic material for thermoelectric applications, particularly in regimes where high thermopower at moderate temperatures is desired. Before analyzing the electrical transport coefficients, it is necessary to clarify the treatment of the carrier relaxation time (τ). In the present work, a constant relaxation time approximation is adopted, with the relaxation time fixed at $\tau = 1 \times 10^{-13}$ s. This choice allows the intrinsic features of the electronic band structure to be isolated from complex scattering mechanisms, enabling a transparent comparison between electron- and hole-doped transport behavior. The selected relaxation time lies within the typical range reported for two-dimensional semiconducting materials and provides physically reasonable magnitudes for conductivity and thermal transport. While the absolute values of the transport coefficients scale linearly with τ, the relative trends with respect to carrier concentration and temperature remain unaffected, ensuring the reliability of the comparative analysis presented below. Fig. 6 depicts the carrier-concentration dependence of (a) electrical conductivity and (b) electronic thermal conductivity of the MoS_2O altermagnet at 300 K, 400 K, and 500 K. In both panels, the transport coefficients vanish at the charge-neutrality point and increase symmetrically with carrier injection, reflecting the semiconducting character of the system and the absence of intrinsic carriers at zero doping. As shown in Fig. 6 (a), the electrical conductivity increases monotonically with carrier concentration for both electron and hole doping. At 300 K, the maximum conductivity reaches approximately $6.9 \times 10^5\ \Omega^{-1}\ m^{-1}$ for the electron-doped regime, whereas a slightly lower value of about $6.0 \times 10^5\ \Omega^{-1}\ m^{-1}$ is obtained for hole doping. This asymmetry originates from the lower effective mass and higher mobility of electrons compared with holes in MoS_2O, leading to more efficient

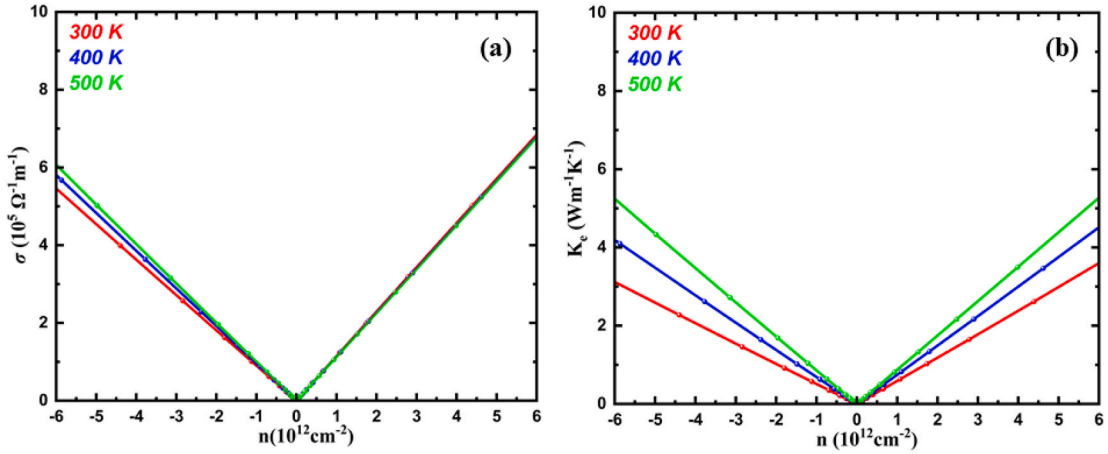

Fig. 6. Carrier-concentration dependence of (a) electrical conductivity and (b) electronic thermal conductivity of the Janus Mo_2S_2O monolayer at 300 K, 400 K, and 500 K.

charge transport under electron injection. With increasing temperature, the conductivity shows a moderate enhancement across the entire carrier concentration range due to the thermally activated population of electronic states. Fig. 6 (b) presents the corresponding electronic contribution to the thermal conductivity (κ_e). Similar to the electrical conductivity, (κ_e) increases with carrier concentration and displays a symmetric trend for electron and hole doping. The electron-doped system exhibits a larger κ_e, reaching a maximum value of approximately 5.5 W m^{-1} K^{-1}, while the hole-doped counterpart attains a slightly smaller value of about 5.1 W m^{-1} K^{-1}. The reduced κ_e in the hole-doped regime is consistent with the larger effective mass of holes, which suppresses carrier velocity and limits heat transport. Additionally, κ_e increases with temperature, reflecting the enhanced thermal energy carried by mobile charge carriers. Overall, the combined behavior of electrical and electronic thermal conductivities highlights the intrinsic carrier-dependent transport asymmetry in MoS_2O and emphasizes the advantage of electron doping for achieving higher electrical performance, while hole doping offers comparatively reduced thermal

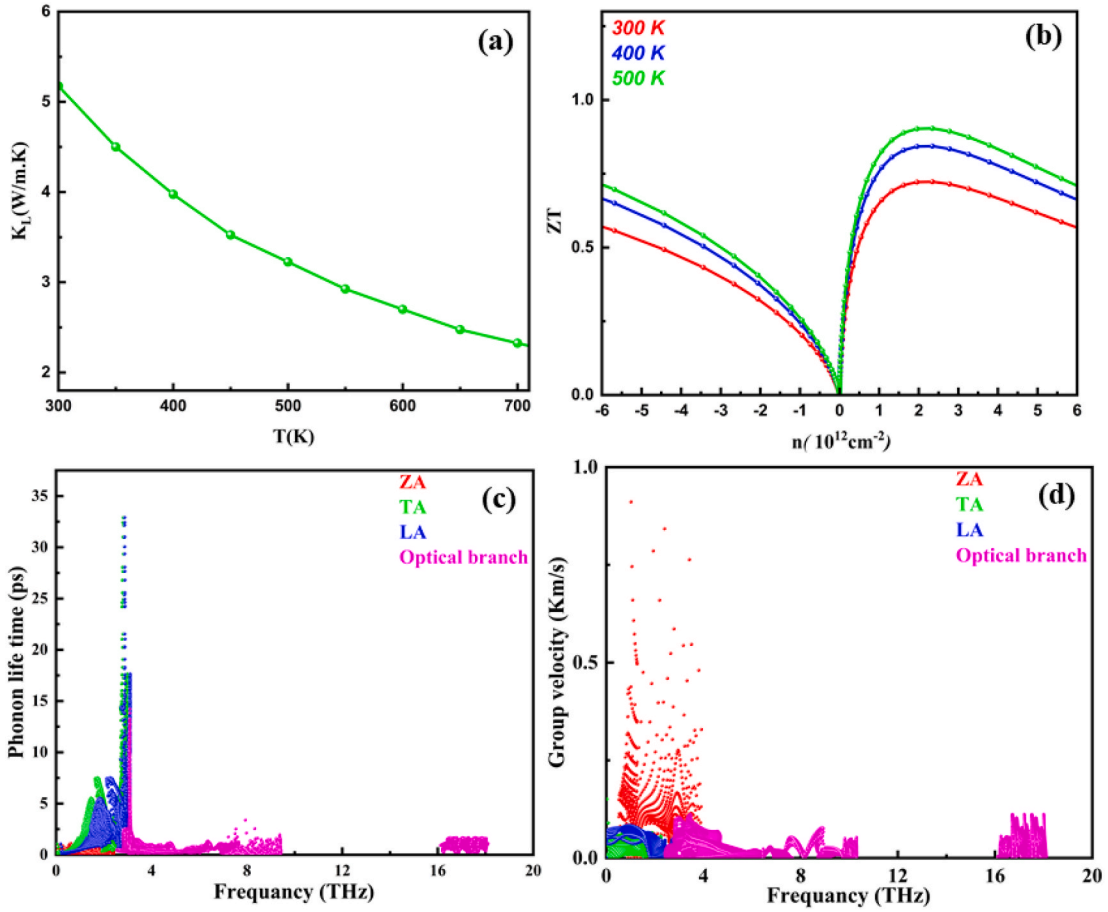

Fig. 7. (a) Temperature dependence of lattice thermal conductivity, (b) carrier concentration dependence of the thermoelectric figure of merit at 300, 400 and 500 K, (c) Phonon lifetime and (d) Group velocity of the Janus Mo_2S_2O monolayer.

transport, which is beneficial for thermoelectric efficiency optimization. Fig. 7 shows (a) the variation of lattice thermal conductivity with temperature and (b) the dependence of the thermoelectric figure of merit (ZT) on carrier concentration for the MoS_2O altermagnet at 300 K, 400 K, and 500 K, providing an overall picture of heat transport and thermoelectric performance. As shown in Fig. 7 (a), the lattice thermal conductivity exhibits a monotonic decrease with increasing temperature, dropping from approximately 5.2 W m^{-1} K^{-1} at 300 K to about 2.3 W m^{-1} K^{-1} at 700 K. This pronounced reduction originates from enhanced phonon–phonon scattering at elevated temperatures, which effectively limits lattice heat transport. The relatively low lattice thermal conductivity at high temperatures is advantageous for thermoelectric performance, as it suppresses parasitic heat flow without directly degrading electrical transport. Similarly, Fig. 7 (b) presents the variation of the dimensionless thermoelectric figure of merit as a function of carrier concentration. The ZT value approaches zero near the charge-neutrality point due to the absence of mobile carriers and increases rapidly upon both electron and hole doping. A clear asymmetry is observed between the two doping regimes, with the electron-doped side exhibiting a higher ZT over the entire carrier concentration range. This enhancement is attributed to the combined effect of larger electrical conductivity and favorable Seebeck response under electron injection. For a fixed carrier concentration, the ZT value increases systematically with temperature, reaching its maximum at 500 K, where the peak ZT exceeds 0.9 in the electron-doped regime. This improvement arises from the simultaneous reduction of lattice thermal conductivity and the thermal activation of charge carriers, which together enhance the power factor relative to total thermal transport. The hole-doped region also shows a noticeable increase in ZT with temperature, although its magnitude remains comparatively lower due to reduced electrical conductivity. Overall, the results demonstrate that MoS_2O combines low lattice thermal conductivity with tunable electronic transport, enabling a substantial thermoelectric figure of merit, particularly under electron doping and elevated temperatures. These findings highlight the promise of altermagnetic MoS_2O as an efficient thermoelectric material for medium-to-high-temperature applications.

To further clarify the origin of the low lattice thermal conductivity, we analyzed the phonon group velocities and phonon lifetimes. The single mode relaxation time (τ_λ) was obtained from the phonon linewidth Γ of the phonon mode λ using the relation [29].

$$\tau_\lambda = \frac{1}{2\Gamma_\lambda \omega_\lambda}$$

The calculated phonon lifetimes (τ_λ) are shown in Fig. 7 (c). The longitudinal acoustic (LA) and transverse acoustic (TA) modes exhibit the longest lifetimes over the low frequency region, indicating weaker phonon scattering for these modes. In contrast, the flexural acoustic (ZA) mode shows a much shorter lifetime, nearly eight times smaller than the acoustic in plane modes at low frequencies, which suggests stronger anharmonic scattering. It is also noted that no optical phonon modes appear in the low frequency region. At higher frequencies, the optical phonon modes display significantly shorter lifetimes compared to the acoustic modes due to enhanced phonon-phonon interactions. These results indicate that heat transport is mainly governed by the LA and TA modes, while the contribution from the ZA mode is strongly suppressed because of its short lifetime. Similarly, optical phonon modes contribute weakly to lattice thermal transport owing to their limited lifetimes. The combined effect of strong anharmonic scattering and reduced phonon lifetimes therefore plays a key role in lowering the lattice thermal conductivity. Next to that we computed the phonon group velocity and results are shown in Fig. 7 (d). In the low frequency region, the acoustic phonon modes dominate the transport behavior. Among them, the longitudinal acoustic mode exhibits the highest group velocity, followed by the transverse acoustic mode, indicating that these modes are the primary carriers of heat. The ZA mode shows comparatively lower group velocities, which is characteristic of two-dimensional systems and reflects its quadratic dispersion near the Γ point. In contrast, the optical phonon modes possess very small group velocities across the entire frequency range due to their nearly flat dispersion relations. As a result, their contribution to lattice thermal transport is limited despite their presence at higher frequencies. The combined effect of reduced group velocity in the flexural mode and the nearly vanishing group velocity of optical modes significantly suppresses phonon heat transport, thereby contributing to the overall low lattice thermal conductivity of the system.

4. Conclusion

In this work, the Janus Mo_2S_2O monolayer is established as a rare two-dimensional platform that integrates altermagnetism, piezoelectricity, piezo-valley polarization, and thermoelectric functionality within a single material. The system exhibits a stable compensated antiferromagnetic ground state, with a Néel temperature close to 550 K, indicating that the magnetic order remains robust across the entire operational temperature range. The electronic structure displays pronounced symmetry-protected spin splitting, while the application of uniaxial strain efficiently lifts the valley degeneracy and generates a giant piezo-valley response, with valley splittings reaching 334 meV. Such strong coupling between lattice deformation and valley polarization provides an effective route for controlling spin-polarized electronic states. In addition to its magnetic and valley-related properties, the polar Janus configuration induces a strong out-of-plane piezoelectric response, enhancing the electromechanical coupling of the monolayer. From an energy-conversion perspective, the combination of a large Seebeck coefficient, suppressed lattice thermal conductivity, and favorable carrier transport leads to a high thermoelectric figure of merit approaching 0.97 at 500 K. The coexistence of robust altermagnetism, strain-tunable piezo-valley polarization, and efficient thermoelectric performance highlights Janus Mo_2S_2O as a promising multifunctional material for next-generation spin-valley electronics and low-temperature waste-heat recovery technologies.

CRediT authorship contribution statement

Fazle Subhan: Conceptualization, Investigation, Methodology, Visualization, Writing – original draft, Writing – review & editing. **Luqman Ali:** Investigation, Writing – original draft, Writing – review & editing. **Zhansheng Lu:** Resources, Writing – original draft, Writing – review & editing. **Joonkyung Jang:** Formal analysis, Funding acquisition, Investigation, Project administration, Supervision, Writing – original draft, Writing – review & editing.

Declaration of competing interest

The authors affirm that the work presented in this paper was not influenced by any known financial interests or personal connections.

Acknowledgments

This work was supported by the Industrial Technology Innovation Program (RS-2024-00435432: Development of hydrogen production technology through ammonia decomposition using a plasmonics-based light system with high performance and long-term durability), funded by the Ministry of Trade Industry & Energy (MOTIE, Korea). This research was supported by Brain Pool program funded by the Ministry of Science and ICT through the National Research Foundation of Korea (RS-2025-25396197).

Data availability

Data will be made available on request.

References

[1] Z.Q. Wang, N.J. Zhou, J. Guo, X.Y. Wang, Fluid selection and parametric optimization of organic Rankine cycle using low temperature waste heat, Energy 40 (1) (2012) 107–115.

[2] D. Wang, X. Ling, H. Peng, L. Liu, L. Tao, Efficiency and optimal performance evaluation of organic Rankine cycle for low grade waste heat power generation, Energy 50 (2013) 343–352.

[3] G.D. Mahan, J.O. Sofo, The best thermoelectric, Proc. Natl. Acad. Sci. 93 (15) (1996) 7436–7439.

[4] F. Hao, P. Qiu, Y. Tang, S. Bai, T. Xing, H.S. Chu, L. Chen, High efficiency Bi 2 Te 3-based materials and devices for thermoelectric power generation between 100 and 300 C, Energy Environ. Sci. 9 (10) (2016) 3120–3127.

[5] S. Singh, K. Hirata, S.K. Pandey, T. Takeuchi, Recent advances in energy harvesting from waste heat using emergent thermoelectric materials, Emerging Materials: Design, Characterization and Applications (2022) 155–184.

[6] J.P. Heremans, M.S. Dresselhaus, L.E. Bell, D.T. Morelli, When thermoelectrics reached the nanoscale, Nat. Nanotechnol. 8 (7) (2013) 471–473.

[7] L.D. Zhao, B.P. Zhang, J.F. Li, M. Zhou, W.S. Liu, J. Liu, Thermoelectric and mechanical properties of nano-sic-dispersed Bi2Te3 fabricated by mechanical alloying and spark plasma sintering, J. Alloys Compd. 455 (1-2) (2008) 259–264.

[8] J. Ding, T. Lanigan-Atkins, M. Calderón-Cueva, A. Banerjee, D.L. Abernathy, A. Said, O. Delaire, Soft anharmonic phonons and ultralow thermal conductivity in Mg3 (Sb, Bi) 2 thermoelectrics, Sci. Adv. 7 (21) (2021).

[9] G.J. Snyder, E.S. Toberer, Complex thermoelectric materials, Nat. Mater. 7 (2) (2008) 105–114.

[10] C.B. Vining, An inconvenient truth about thermoelectrics, Nat. Mater. 8 (2) (2009) 83–85.

[11] S. Basak, S.R. Nagel, B.C. Giessen, Thermoelectric power of magnetic and nonmagnetic amorphous metals, Phys. Rev. B 21 (9) (1980) 4049.

[12] A. Bentien, G.K.H. Madsen, S. Johnsen, B.B. Iversen, Experimental and theoretical investigations of strongly correlated FeSb 2− x Sn x, Phys. Rev. B Condens. Matter 74 (20) (2006): 205105.

[13] N. Tsujii, T. Mori, High thermoelectric power factor in a carrier-doped magnetic semiconductor CuFeS2, APEX 6 (4) (2013): 043001.

[14] H. Takaki, K. Kobayashi, M. Shimono, N. Kobayashi, K. Hirose, N. Tsujii, T. Mori, Thermoelectric properties of a magnetic semiconductor CuFeS2, Mater. Today Phys. 3 (2017) 85–92.

[15] H. Takahashi, R. Okazaki, S. Ishiwata, H. Taniguchi, A. Okutani, M. Hagiwara, I. Terasaki, Colossal seebeck effect enhanced by quasi-ballistic phonons dragging massive electrons in FeSb2, Nat. Commun. 7 (1) (2016): 12732.

[16] K.I. Uchida, H. Adachi, T. Kikkawa, A. Kirihara, M. Ishida, S. Yorozu, E. Saitoh, Thermoelectric generation based on spin seebeck effects, Proc. IEEE 104 (10) (2016) 1946–1973.

[17] T. Mori, Novel principles and nanostructuring methods for enhanced thermoelectrics, Small 13 (45) (2017): 1702013.

[18] W. Zhao, Z. Liu, P. Wei, Q. Zhang, W. Zhu, X. Su, Y. Pei, Magnetoelectric interaction and transport behaviours in magnetic nanocomposite thermoelectric materials, Nat. Nanotechnol. 12 (1) (2017) 55–60.

[19] T. Mori, S. Priya, Materials for energy harvesting: at the forefront of a new wave, MRS Bull. 43 (3) (2018) 176–180.

[20] N. Tsujii, A. Nishide, J. Hayakawa, T. Mori, Observation of enhanced thermopower due to spin fluctuation in weak itinerant ferromagnet, Sci. Adv. 5 (2) (2019).

[21] S. Liu, M. Chen, C. Fu, T. Zhu, The interplay of magnetism and thermoelectricity: a review, Advanced Physics Research 2 (9) (2023): 2300015.

[22] S. Singh, N. Liu, Y. Zhang, A. Nozariasbmarz, S.K. Karan, L. Raman, B. Poudel, High-performance thermomagnetic Gd–Si–Ge alloys, ACS Appl. Mater. Interfaces 15 (29) (2023) 35140–35148.

[23] S. Singh, B. Poudel, A. Nozariasbmarz, T. Takeuchi, S. Priya, Constructive approach towards design of high-performance thermoelectrics, thermal diodes, and thermomagnetic devices for energy generation applications, in: Energy Harvesting and Storage Devices, CRC Press, 2023, pp. 80–107.

[24] J.B. Vaney, S.A. Yamini, H. Takaki, K. Kobayashi, N. Kobayashi, T. Mori, Magnetism-mediated thermoelectric performance of the Cr-doped bismuth telluride tetradymite, Mater. Today Phys. 9 (2019): 100090.

[25] Y. Wu, Z. Chen, P. Nan, F. Xiong, S. Lin, X. Zhang, Y. Pei, Lattice strain advances thermoelectrics, Joule 3 (5) (2019) 1276–1288.

[26] G. Yang, L. Sang, C. Zhang, N. Ye, A. Hamilton, M.S. Fuhrer, X. Wang, The role of spin in thermoelectricity, Nat. Rev. Phys. 5 (8) (2023) 466–482.

[27] L. Hu, K.Z. Du, Y. Chen, Y. Zhai, X. Wang, Q. Xiong, Spin-phonon coupling in two-dimensional magnetic materials, National Science Open 2 (4) (2023): 20230002.

[28] C. Song, H. Bai, Z. Zhou, L. Han, H. Reichlova, J.H. Dil, F. Pan, Altermagnets as a new class of functional materials, Nat. Rev. Mater. (2025) 1–13.

[29] X. Zhou, W. Feng, R.W. Zhang, L. Šmejkal, J. Sinova, Y. Mokrousov, Y. Yao, Crystal thermal transport in altermagnetic RuO 2, Phys. Rev. Lett. 132 (5) (2024): 056701.

[30] X. Chen, D. Wang, L. Li, B. Sanyal, Room temperature two-dimensional antiferromagnetic Weyl semimetal CrO with giant spin-splitting and spin-momentum locked transport, arXiv preprint arXiv:2104.07390 (2021).

[31] P.J. Guo, Z.X. Liu, Z.Y. Lu, Quantum anomalous hall effect in collinear antiferromagnetism, npj Comput. Mater. 9 (1) (2023) 70.

[32] H.Y. Ma, M. Hu, N. Li, J. Liu, W. Yao, J.F. Jia, J. Liu, Multifunctional antiferromagnetic materials with giant piezomagnetism and noncollinear spin current, Nat. Commun. 12 (1) (2021) 2846.

[33] S.D. Guo, Valley polarization in two-dimensional zero-net-magnetization magnets, Appl. Phys. Lett. 126 (8) (2025).

[34] H. Siddiq, Coupled piezovalley, piezoelectric, and thermoelectric effects in Janus Cr2STe altermagnet, J. Phys. Chem. Solid. (2025): 113514.

[35] S.D. Guo, Hidden altermagnetism, arXiv preprint arXiv:2411.13795 (2024).

[36] J. Hafner, Ab-initio simulations of materials using VASP: density-functional theory and beyond, J. Comput. Chem. 29 (13) (2008) 2044–2078.

[37] A. Jain, G. Hautier, S.P. Ong, C.J. Moore, C.C. Fischer, K.A. Persson, G. Ceder, Formation enthalpies by mixing GGA and GGA+ U calculations, Phys. Rev. B Condens. Matter 84 (4) (2011): 045115.

[38] A. Togo, First-principles phonon calculations with phonopy and phono3py, J. Phys. Soc. Jpn. 92 (1) (2023): 012001.

[39] G.K. Madsen, D.J. Singh, BoltzTraP. A code for calculating band-structure dependent quantities, Comput. Phys. Commun. 175 (1) (2006) 67–71.

[40] S.M. Al-Shomar, M. Liaqat, I. Anmol, A.M. Quraishi, I. Khan, K. Arshad, A. Zaman, Study of structural, electronic, mechanical, optical and thermoelectric properties of as based halide-perovskites Ba3AsX3 (X= F, Cl): a first-principles insights, J. Mater. Res. Technol. 31 (2024) 2450–2460.

[41] J. Krempaský, L. Šmejkal, S.W. D'souza, M. Hajlaoui, G. Springholz, K. Uhlířová, T. Jungwirth, Altermagnetic lifting of Kramers spin degeneracy, Nature 626 (7999) (2024) 517–522.

[42] O. Gomonay, V.P. Kravchuk, R. Jaeschke-Ubiergo, K.V. Yershov, T. Jungwirth, L. Šmejkal, J. Sinova, Structure, control, and dynamics of altermagnetic textures, npj Spintronics 2 (1) (2024) 35.

[43] Y. Chang, Y. Wu, L. Deng, X. Yin, X. Zhang, Valley-related multipiezo effect in altermagnet monolayer V2STeO, Materials 18 (3) (2025) 527.

[44] A. Zaman, K. Husain, S.H. Alrefaee, H. Shahid, M. Elhadi, A. Nurmuhammedov, N. Elboughdiri, Multipiezo effect in altermagnet V2SeO monolayer at high temperature, Case Stud. Therm. Eng. (2025): 106943.

[45] Q. Ma, B. Wang, G. Yang, Y. Liu, Multifunctional altermagnet with large out-of-plane piezoelectric response in Janus V2AsBrO monolayer, Appl. Phys. Lett. 126 (22) (2025).

[46] S.D. Guo, X.S. Guo, K. Cheng, K. Wang, Y.S. Ang, Piezoelectric altermagnetism and spin-valley polarization in Janus monolayer Cr2SO, Appl. Phys. Lett. 123 (8) (2023).